Aero-optics of subsonic turbulent boundary layers

Kan Wang and Meng Wang†

Institute for Flow Physics and Control, Department of Aerospace and Mechanical Engineering,
University of Notre Dame, Notre Dame, IN 46556, USA

Compressible large-eddy simulations are carried out to study the aero-optical distortions caused by Mach 0.5 flat-plate turbulent boundary layers at Reynolds numbers of $Re_\theta = 875$, 1770 and 3550, based on momentum thickness. The fluctuations of refractive index are calculated from the density field, and wavefront distortions of an optical beam traversing the boundary layer are computed based on geometric optics. The effects of aperture size, small-scale turbulence, different flow regions and beam elevation angle are examined and the underlying flow physics is analysed. It is found that the level of optical distortion decreases with increasing Reynolds number within the Reynolds-number range considered. The contributions from the viscous sublayer and buffer layer are small, while the wake region plays a dominant role, followed by the logarithmic layer. By low-pass filtering the fluctuating density field, it is shown that small-scale turbulence is optically inactive. Consistent with previous experimental findings, the distortion magnitude is dependent on the propagation direction due to anisotropy of the boundary-layer vortical structures. Density correlations and length scales are analysed to understand the elevation-angle dependence and its relation to turbulence structures. The applicability of Sutton's linking equation to boundary-layer flows is examined, and excellent agreement between linking equation predictions and directly integrated distortions is obtained when the density length scale is appropriately defined.

Key words: boundary layers, compressible flows, turbulence simulation

1. Introduction

The aero-optical phenomenon refers to distortions of optical signals by turbulent flows adjacent to a projection or viewing aperture. In a compressible turbulent flow, density fluctuations cause fluctuations in the index-of-refraction field. When an initially collimated optical wavefront is transmitted through a turbulent flow over the aperture, it is distorted due to the non-uniform speed of light in the medium. Such distortions can cause severe problems such as beam jitter, image blur and loss of intensity in the far field. Aero-optical distortions are detrimental to airborne communication, targeting, imaging and directed energy systems (Jumper & Fitzgerald 2001).

The optical aberrations induced by turbulent boundary layers have been studied extensively since the 1950s (Liepmann 1952). Earlier investigations were primarily

† Email address for correspondence: M.Wang@nd.edu

experimental. Limited by experimental techniques, measurements up to 1980 were focused on time-averaged optical distortions (Geary & Otten 1982). The development of wavefront sensors at high sampling speed since the late 1980s enabled the dynamic measurement of optical distortions in time and space, and hence detailed analysis of distortion structure and mechanisms. The most commonly used wavefront sensors are Malley probes and Shack–Hartmann sensors. The former measure the wavefront slope at a single spatial location as a function of time, and a one-dimensional wavefront is then reconstructed based on Taylor's hypothesis (Malley, Sutton & Kincheloe 1992). A two-dimensional Shack–Hartmann wavefront sensor is designed according to Huygens' principle and utilizes a lenslet array to record two-dimensional wavefronts (Geary 1995).

With Malley probes, Gordeyev *et al.* (2003), Buckner, Gordeyev & Jumper (2005), Wittich, Gordeyev & Jumper (2007) and Cress *et al.* (2008) conducted a series of experiments to study the optical effects of turbulent boundary layers over the Mach number range of 0.3–0.95 and Reynolds number range of 34 000–42 500 based on the momentum thickness. They examined statistical properties of optical distortions and proposed a scaling law for the magnitude of optical path difference, OPD_{rms} (the definition of OPD will be given in § 2.2), which was shown to be proportional to the boundary-layer displacement thickness, the free-stream density and the square of the free-stream Mach number. Cress *et al.* (2008) performed measurements of aero-optical properties of turbulent boundary layers at different beam elevation angles and found that the beam experienced larger distortions when it was tilted towards the downstream direction than those when it was tilted upstream. They pointed out that the elevation angle effect was caused by the large anisotropic coherent structures in boundary layers. The effects of heated and cooled walls were examined by Cress, Gordeyev & Jumper (2010). It was found that optical distortions can be significantly reduced when the upstream wall was cooled appropriately.

Wyckham & Smits (2009) measured optical distortions by transonic and hypersonic boundary layers with a two-dimensional Shack–Hartmann wavefront sensor. Based on the strong Reynolds analogy and by assuming negligible pressure fluctuations, they proposed a new scaling law for OPD_{rms} which depends on the local skin-friction coefficient and thereby Reynolds number. According to their scaling law, OPD_{rms} is proportional to the free-stream density, boundary-layer thickness, square of the free-stream Mach number and the square-root of the local skin-friction coefficient. The scaling law also involved the ratio of bulk to free-stream temperatures and a coefficient which was found to have only small variations over the Mach-number range from 0.8 to 7.8. A similar scaling law was later obtained by Gordeyev, Jumper & Hayden (2011). The two-dimensional wavefront sensor allowed a direct measurement of two-point spatial correlations of OPD, from which Wyckham & Smits (2009) found comparable correlation lengths in the streamwise and spanwise directions for subsonic boundary layers, in contrast to the streamwise-elongated correlations noted by Wittich *et al.* (2007) based on Malley probe measurements at higher Reynolds numbers.

Computations of aero-optics can be traced back to the late 1980s. Early computational studies involved two-dimensional solutions of the Euler equations (Tsai & Christiansen 1990) or Reynolds-averaged Navier–Stokes (RANS) equations (Cassady, Birch & Terry 1989). Recent advances in high-fidelity simulation techniques, including direct numerical simulation (DNS), large-eddy simulation (LES) and hybrid RANS/LES methods, have led to a significant growth in numerical investigations of aero-optical phenomena and improved predictive capabilities. Together with experiments, these investigations provided new physical understanding of the distortion

mechanisms of various aero-optical flows including turbulent boundary layers. A detailed discussion of aero-optical computations can be found in the review article of Wang, Mani & Gordeyev (2012).

Truman & Lee (1990) and Truman (1992) used incompressible DNS to study the optical distortions induced by a homogeneous turbulent shear flow with uniform mean shear and a turbulent channel flow. The fluctuating index of refraction was modelled as a passive scalar. They observed that optical distortions were significantly dependent on the propagation direction, and related the distortions to the underlying coherent vortical structures. It was found that larger distortions occurred when the beam was propagated at an angle close to the inclination angle of hairpin vortices. Truman (1992) further pointed out that optical distortions were dominated by large-scale vortical structures, and thus their directionality was strongly affected by the anisotropy of the organized vortical structures. Although these studies did not deal with turbulent boundary layers and were based on incompressible flow equations, the major results are similar to those found from subsequent boundary-layer experiments (Cress *et al.* 2008) and the present compressible flow simulation (see § 7).

Mani, Wang & Moin (2006) and Mani, Moin & Wang (2009) simulated flow over a circular cylinder at Reynolds numbers of 3900 and 10 000 and Mach number of 0.4 with a sixth-order, non-dissipative LES code and investigated the aero-optical effects of separated shear layers and turbulent wakes. They analysed systematically the far-field optical statistics and their dependence on optical wavelength, aperture size, and beam position in the flow field. They also examined the effect of different flow scales on aero-optics and, based on statistical theory for small-scale turbulence, established a grid-resolution criterion for accurately capturing the aero-optical effects (Mani, Wang & Moin 2008). The basic conclusion is that an adequately resolved LES can capture the aero-optics of highly aberrating flows without requiring additional subgrid-scale modelling for the optics.

Tromeur *et al.* (2003) and Tromeur, Garnier & Sagaut (2006*b*) carried out LES to study the aero-optical distortions of subsonic ($M = 0.9$) and supersonic ($M = 2.3$) flat-plate turbulent boundary layers. Their result for $M = 0.9$ was in reasonable agreement with experimental data in terms of the optical-phase-distortion magnitude. The convection velocities of optical aberrations for both cases were found to be approximately 0.8 times the free-stream velocity, which was consistent with the experimental findings of Buckner *et al.* (2005). They evaluated the applicability of Sutton's statistical model (Sutton 1985), known as the linking equation which relates the mean square of optical phase distortions to density variance and correlation length under simplifying assumptions, by comparing the computed results to Sutton's model predictions. Significant discrepancies were observed between the two results for both Mach numbers and, as a result, they questioned the applicability of Sutton's model for boundary-layer flows. In a follow-up study, Tromeur, Garnier & Sagaut (2006*a*) found satisfactory predictions of OPD by Sutton's model based on the velocity correlation length instead of density correlation length. This is, however, difficult to justify from a theoretical standpoint.

Despite previous experimental and numerical studies on aero-optics of turbulent boundary layers, the results in the literature are scattered and sometimes contradictory. A clear understanding of boundary-layer aero-optical phenomena is still lacking. The objective of the current work is to contribute to a systematic understanding of optical-distortion mechanisms induced by subsonic turbulent boundary layers. To this end highly resolved compressible LES is performed for Mach 0.5 turbulent boundary layers at Reynolds numbers of $Re_\theta = 875$, 1770 and 3550 based on the momentum

thickness at the centre of the optical aperture, and the index-of-refraction field is computed directly from the fluctuating density field for optical analysis. Important issues, such as Reynolds-number dependence of OPD, contributions from different flow regions and flow scales to the wavefront aberrations, and the dependence on propagation direction are examined. Flow structures, especially structures of the fluctuating density field, are analysed and related to the optical distortions. The applicability of Sutton's linking equation to boundary-layer flows is revisited, and the appropriate definition of the density length scale in the equation is clarified. Based on the correct definition, the density correlation lengths at different elevation angles are calculated, and the elevation-angle dependence of optical distortions is explained in terms of the correlation length and the underlying flow structures.

The paper is organized as follows. Section 2 describes the numerical methods for LES and optical calculations. Section 3 presents the results of flow simulation and compares basic statistics to available experimental data. Instantaneous wavefront distortions and time-averaged distortion magnitudes are shown in §4, which also discusses their Reynolds-number dependence and contributions from different flow regions and flow scales. Section 5 presents the structure of wavefront distortions in terms of two-point correlations and space–time correlations of OPD. The applicability of Sutton's linking equation to boundary-layer flows is analysed in §6, and the appropriate density correlation length is identified. The effect of elevation angle on optical distortions is examined in §7 based on the linking equation and correlation length distribution. Finally, §8 summarizes the main conclusions of this work.

2. Numerical approach

The aero-optical study is performed in two steps: first, LES is conducted to provide a detailed description of the turbulent flow field including the fluctuating density field; second, the refractive index is obtained from the Gladstone–Dale relation (Gladstone & Dale 1863) and optical calculations are performed on a beam grid to compute the optical wavefront distortions.

2.1. *Large-eddy simulation*

The governing equations for LES are the spatially filtered compressible Navier–Stokes equations and the continuity and energy equations in the following dimensionless and conservative form (see, for example, Garnier, Adams & Sagaut 2009):

$$\frac{\partial \bar{\rho}}{\partial t} + \frac{\partial \bar{\rho}\widetilde{u}_j}{\partial x_j} = 0, \tag{2.1}$$

$$\frac{\partial \bar{\rho}\widetilde{u}_i}{\partial t} + \frac{\partial}{\partial x_j}(\bar{\rho}\widetilde{u}_i\widetilde{u}_j + \bar{p}\delta_{ij}) = \frac{\partial \widetilde{\tau}_{ij}}{\partial x_j} - \frac{\partial \tau_{ij}^{SGS}}{\partial x_j}, \tag{2.2}$$

$$\frac{\partial \bar{\rho}\widetilde{E}}{\partial t} + \frac{\partial}{\partial x_j}\left[(\bar{\rho}\widetilde{E} + \bar{p})\widetilde{u}_j\right] = \frac{\partial \bar{q}_j}{\partial x_j} + \frac{\partial}{\partial x_k}(\widetilde{u}_j\widetilde{\tau}_{jk}) - \frac{\partial q_j^{SGS}}{\partial x_j}, \tag{2.3}$$

where ρ, p, T, u_i and E denote density, pressure, temperature, the three velocity components and total energy, respectively, normalized using boundary-layer thickness δ, free-stream density ρ_∞, sound speed c_∞, temperature T_∞ and dynamic viscosity μ_∞ as reference values. The overbar denotes spatial filtering and the tilde denotes

Favre filtering,

$$\widetilde{f} = \frac{\overline{\rho f}}{\bar{\rho}}. \tag{2.4}$$

The Favre-filtered viscous stress tensor is given by

$$\widetilde{\tau}_{ij} = \frac{\mu M}{Re} \left(\frac{\partial \widetilde{u}_i}{\partial x_j} + \frac{\partial \widetilde{u}_j}{\partial x_i} - \frac{2}{3} \frac{\partial \widetilde{u}_k}{\partial x_k} \delta_{ij} \right), \tag{2.5}$$

and the filtered heat flux is

$$\bar{q}_j = \frac{\mu}{(\gamma - 1)Pr} \frac{\partial \overline{T}}{\partial x_j}, \tag{2.6}$$

where $Re = \rho_\infty u_\infty \delta / \mu_\infty$ is the Reynolds number, $M = u_\infty / c_\infty$ is the Mach number, γ is the ratio of specific heats, and Pr is the Prandtl number. The governing equations (2.1)–(2.3) are supplemented with the equation of state for ideal gas, $\bar{p} = \bar{\rho} \widetilde{T} / \gamma$. The dynamic viscosity μ is a function of T in the form of $\mu = T^n$, where n is assumed a constant ($n = 0.7$ in the present work). The quantities τ_{ij}^{SGS} and q_i^{SGS} in (2.1)–(2.3) are the subgrid-scale (SGS) stress tensor and heat flux, respectively:

$$\tau_{ij}^{SGS} = \bar{\rho}(\widetilde{u_i u_j} - \widetilde{u}_i \widetilde{u}_j), \tag{2.7}$$

$$q_j^{SGS} = \bar{\rho}(\widetilde{u_j T} - \widetilde{u}_j \widetilde{T}), \tag{2.8}$$

which account for the effects of subgrid-scale motions to be modelled in order to close the equations.

The simulation code used in the present study is an unstructured-mesh compressible LES code developed at the Center for Turbulence Research, Stanford University (Shoeybi *et al.* 2010). The code solves the spatially filtered compressible Navier–Stokes equations, (2.1)–(2.3), along with the state equation using low-dissipative, robust numerical algorithms. It employs a second-order finite-volume scheme with a summation-by-parts (SBP) property for spatial discretization and a hybrid implicit/explicit third-order Runge–Kutta method for time advancement. The SGS terms in (2.1) are modelled using the dynamic Smagorinsky model (Moin *et al.* 1991) with Lilly's modification (Lilly 1992).

2.2. *Optical calculation*

As electromagnetic waves, the propagation of optical beams is governed by the Maxwell equations. For aero-optical problems, however, the three components of the electromagnetic field are decoupled because the optical wavelength is much shorter than the smallest flow scale, and thus the Maxwell equations can be reduced to a vector wave equation in which each scalar component of the electric field at frequency ω can be written as

$$\nabla^2 U + \frac{\omega^2 n^2}{c_0^2} U = 0, \tag{2.9}$$

where c_0 is the speed of light in vacuum and n is the index of refraction. Owing to the small fluctuations in index of refraction and much longer flow scales compared to the optical wavelength, the propagation direction of an optical beam is predominantly in the axial (y) direction and the amplitude varies slowly through the turbulence region, so that the wave equation can be parabolized (Monin & Yaglom 1975; Mani *et al.*

2006). The solution of the paraxial wave equation across the aero-optical region (from $y = 0$ to $y = L$) can be expressed as (Monin & Yaglom 1975)

$$U(x, L, z) = U(x, 0, z) \exp\left(-\mathrm{i}k_0 \int_0^L n(x, y, z) \, \mathrm{d}y\right), \qquad (2.10)$$

where $k_0 = k/n_\infty = \omega/c_0$ is the optical wavenumber in vacuum. This equation suggests that the amplitude of the optical waves remains unchanged after transmission through the turbulence region, and the dominant effect on the wavefront is a phase distortion. The integral in (2.10) is called the optical path length (OPL),

$$\mathrm{OPL}(x, z, t) = \int_0^L n(x, y, z, t) \, \mathrm{d}y, \qquad (2.11)$$

and is most commonly derived from geometric optics by assuming straight optical paths. In air flows, the optical index of refraction is related to the fluctuating density field through the Gladstone–Dale relation (Gladstone & Dale 1863)

$$n = 1 + K_{GD}\rho, \qquad (2.12)$$

where K_{GD} is the Gladstone–Dale constant which is in general weakly dependent on the optical wavelength. It is nearly independent of the wavelength and is approximately 2.27×10^{-4} m^3 kg^{-1} for air at visible optical wavelengths.

Optical calculations are generally performed on a Cartesian beam grid along the optical path with its dimensions in the plane perpendicular to the optical path the same as the aperture size. For the current work, since the LES mesh is Cartesian, the optical beam grid is the same as the LES grid but covers a smaller region for propagation normal to the wall. When the beam is at an oblique angle with respect to the wall, the beam grid does not coincide with the LES grid, and a trilinear interpolation scheme is employed to interpolate the density field from the LES grid onto the beam grid.

The relative difference in OPL over the aperture is called the optical path difference (OPD) and is defined as

$$\mathrm{OPD}(x, z, t) = \mathrm{OPL}(x, z, t) - \langle \mathrm{OPL}(x, z, t) \rangle, \qquad (2.13)$$

where the angle brackets denote spatial averaging over the aperture. This quantity is the most frequently used measure of optical distortions. In practice, the spatially linear component of wavefront distortions, called the unsteady tilt, can be corrected using adaptive-optic systems (Tyson 1997) and is therefore removed along with $\langle \mathrm{OPL}(x, z, t) \rangle$ by a least-square surface fitting method. At each time instant, parameters A, B and C are determined by minimizing

$$G = \int \int_{A_p} [\mathrm{OPL}(x, z, t) - (Ax + Bz + C)]^2 \, \mathrm{d}x \, \mathrm{d}z \qquad (2.14)$$

where A_p denotes the aperture, and then $\mathrm{OPD}(x, z, t)$ is computed from

$$\mathrm{OPD}(x, z, t) = \mathrm{OPL}(x, z, t) - (Ax + Bz + C). \qquad (2.15)$$

3. Flow simulation and validation

Spatially developing flat-plate boundary-layer simulations with an inflow–outflow configuration at three Reynolds numbers $Re_\theta = 700$, 1400 and 2800 based on the momentum thickness at the inlet are conducted to investigate optical distortions. The free-stream Mach number is $M = 0.5$. These simulations employ a computational

Re_θ at inlet	Re_θ at beam centre	Beam centre (x, z)	No. of grid cells
700	875	$15.4\delta_0, 1.55\delta_0$	3.8×10^6
1400	1770	$20.1\delta_0, 1.55\delta_0$	1.3×10^7
2800	3550	$21.2\delta_0, 1.55\delta_0$	4.9×10^7

TABLE 1. Flow and optical simulation parameters.

domain of size $31\delta_0$, $6.4\delta_0$ and $3.1\delta_0$ in the streamwise (x), wall normal (y) and spanwise (z) directions, respectively, where δ_0 is the boundary-layer thickness at the inlet. A Cartesian mesh, uniform in the streamwise and spanwise directions and stretched in the wall-normal direction, is employed. The grid spacings in viscous wall units are $\Delta x^+ \approx 30$, $\Delta z^+ \approx 10$ and $\Delta y^+_{min} \approx 0.6$ based on inlet conditions. This grid resolution is significantly better than the typical LES resolution, and is in fact between typical LES and DNS values to ensure sufficient numerical accuracy for a fundamental scientific investigation. The number of grid cells for the three Reynolds numbers are 3.8×10^6, 1.3×10^7 and 4.9×10^7, respectively. No-slip and adiabatic boundary conditions are imposed at the bottom wall. A sponge layer (Israeli & Orszag 1981; Bodony 2006) with thickness of $1.3\delta_0$ is applied to the top and outlet boundaries to damp out flow structures and acoustic waves. The time-dependent turbulent inflow data are generated by a separate simulation adopting an extension of the rescale-and-recycle technique of Lund, Wu & Squires (1998) to compressible flows (Urbin & Knight 2001). A fixed CFL number of 1.0 is employed for time advancement, and variable time steps are calculated accordingly. The typical time step sizes are approximately $8.3 \times 10^{-4}\delta_0/U_\infty$, $5.4 \times 10^{-4}\delta_0/U_\infty$ and $3.0 \times 10^{-4}\delta_0/U_\infty$ for $Re_\theta = 700$, 1400 and 2800, respectively.

A rectangular aperture is employed for optical calculations. The beam centres, listed in table 1, are selected such that at these locations the boundary-layer thickness δ has the same value of $1.36\delta_0$ for all three cases to ensure reasonable comparisons of results at different Reynolds numbers. The Reynolds numbers at the beam centres are $Re_\theta = 875, 1770$ and 3550, respectively, for the three simulations. Hereafter, the beam-centre Reynolds number will be used to characterize the flow in lieu of the Reynolds numbers at the inlet. The main simulation parameters are summarized in table 1. The statistics of flow and optical quantities are calculated over a time period of approximately $196\delta_0/U_\infty$ for $Re_\theta = 875$, $146\delta_0/U_\infty$ for $Re_\theta = 1770$ and $106\delta_0/U_\infty$ for $Re_\theta = 3550$, respectively.

The mean velocity profiles at the beam centres are shown in figure 1 for the three Reynolds numbers, where the coordinates are defined as $y^+ = u_\tau y/\nu$ and $U^+ = U/u_\tau$ (u_τ is the friction velocity). For later reference, the y-coordinate in wall units is related to that measured by the outer scale through $y^+ = (y/\delta)Re_\tau$, with $Re_\tau = 355$, 644 and 1141 for $Re_\theta = 875, 1770$ and 3550, respectively. The profiles coincide with $U^+ = y^+$ in the viscous sublayer and show very good agreement with the log law, indicating the high quality of simulation results. The root-mean-square (r.m.s.) values of velocity fluctuations are plotted in figure 2. For $Re_\theta = 1770$ and 3550, the r.m.s. values of u' and v' are compared with the experimental measurements of DeGraaff & Eaton (2000) at $Re_\theta = 1430$ and 2900 (the closest match to the current Reynolds numbers found), respectively, which shows good agreement.

Figure 3 shows profiles of r.m.s. density fluctuations across the boundary layers. The location of the fluctuation peak in wall units is seen to be insensitive to Reynolds
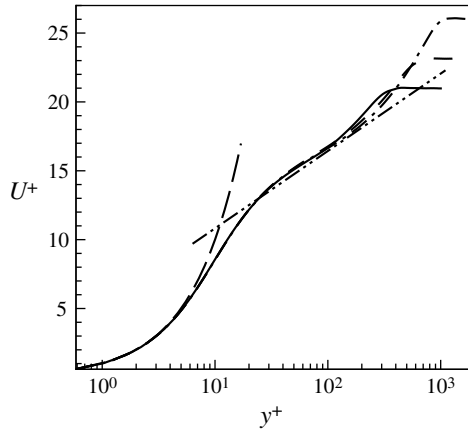
FIGURE 1. Mean velocity profiles at the centre of the aperture. ——, $Re_\theta = 875$; ----, $Re_\theta = 1770$; —·—, $Re_\theta = 3550$; ---, $U^+ = y^+$; -··-, $U^+ = 2.44 \ln y^+ + 5.2$.
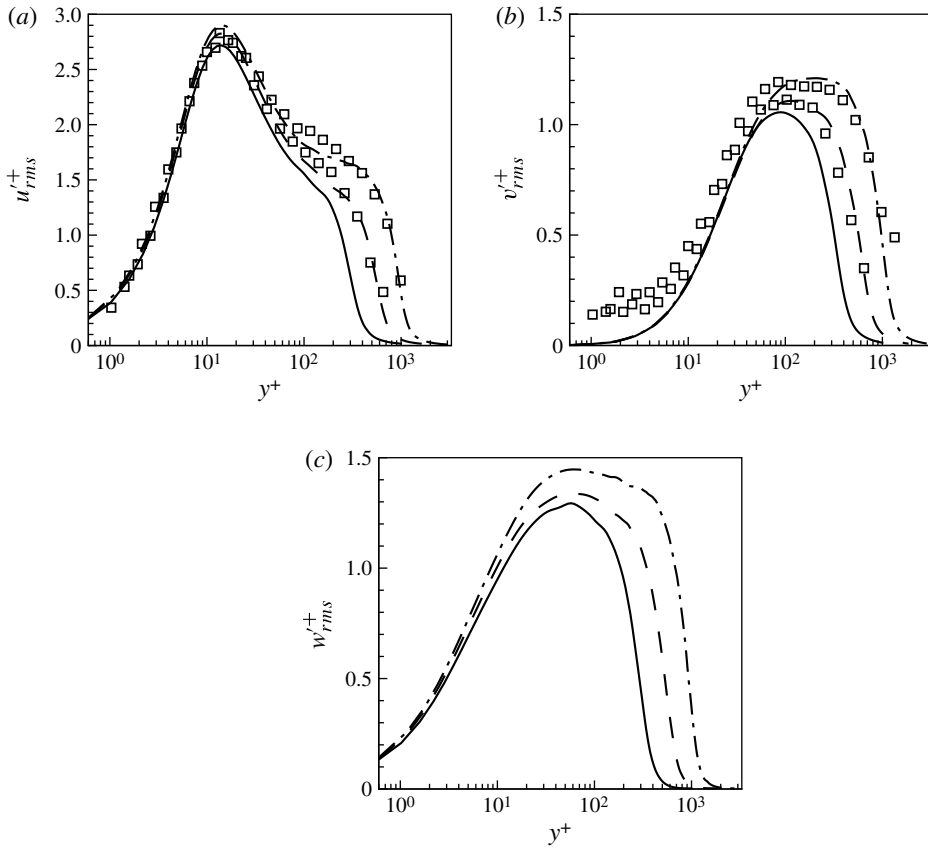

FIGURE 2. Root-mean-square of velocity fluctuations at the centre of the aperture. ——, $Re_\theta = 875$; ----, $Re_\theta = 1770$; —·—, $Re_\theta = 3550$; symbols, from experiment of DeGraaff & Eaton (2000) at $Re_\theta = 1430$ and 2900.
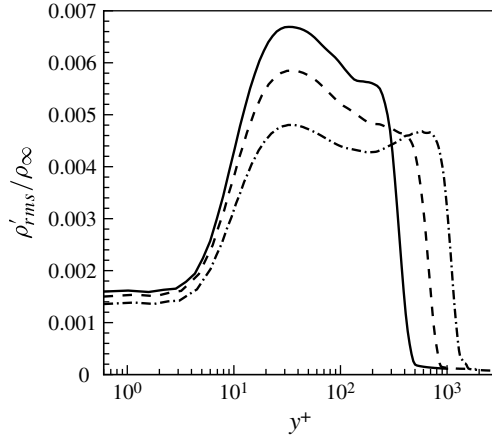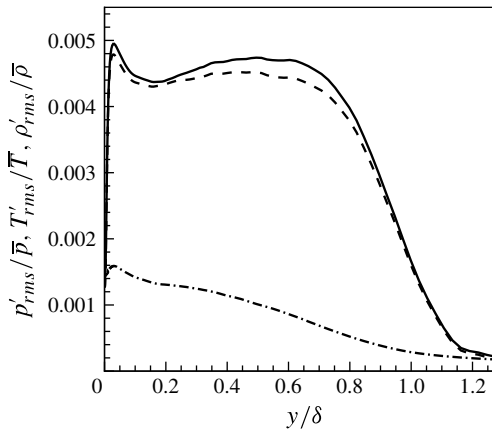
FIGURE 3. Root-mean-square of density fluctuations at the centre of the aperture. ——, $Re_\theta = 875$; - - - -, $Re_\theta = 1770$; $-\cdot-$, $Re_\theta = 3550$.

FIGURE 4. Root-mean-square of density, temperature and pressure fluctuations at the centre of the aperture for $Re_\theta = 3550$. ——, $\rho'_{rms}/\overline{\rho}$; - - - -, $T'_{rms}/\overline{T}$; $-\cdot-$, $p'_{rms}/\overline{p}$.

number and is near the lower end of the logarithmic layer. As Reynolds number increases, the peak fluctuation level decreases, and there is a significant growth in fluctuations in the outer region of the boundary layer. A comparison of the fluctuation magnitudes of density, temperature and pressure relative to their local mean values is shown in figure 4 for $Re_\theta = 3550$. It confirms that, as generally believed (Wyckham & Smits 2009), pressure fluctuations are weak in the turbulent boundary layer, and density fluctuations are primarily caused by temperature fluctuations through the equation of state. Therefore, temperature variations are the main source of optical distortions in the boundary layer, in contrast to the distortion mechanism in turbulent mixing layers where strong pressure variations in coherent vortices play a dominant role (Fitzgerald & Jumper 2004).
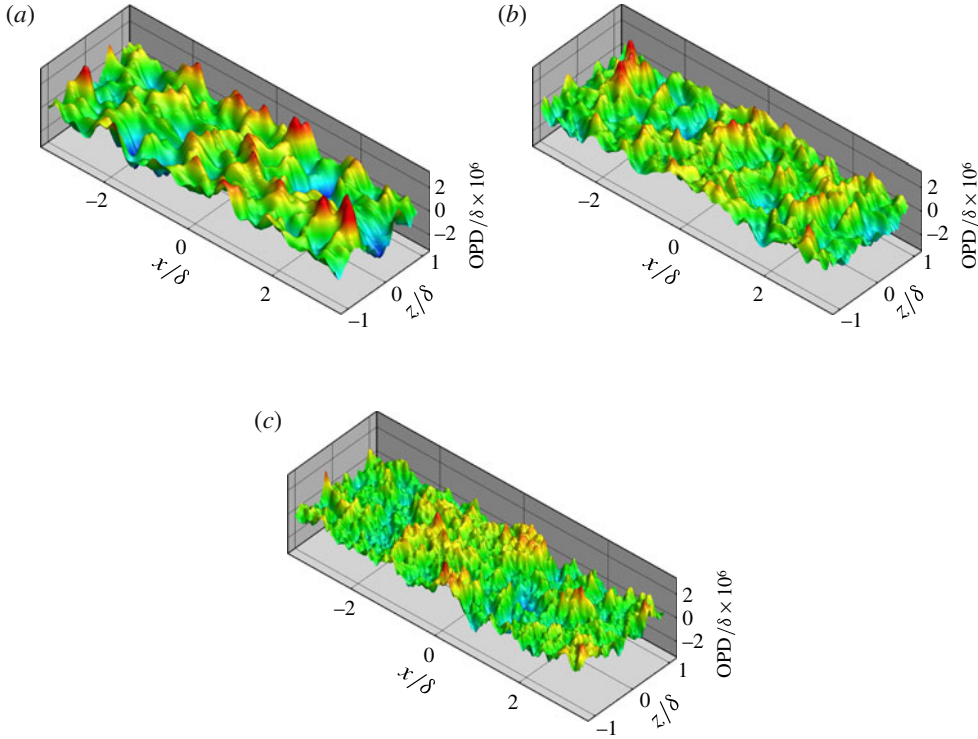
FIGURE 5. Instantaneous OPD at a time instant for different Reynolds numbers: (a) $Re_\theta = 875$; (b) $Re_\theta = 1770$; (c) $Re_\theta = 3550$.

4. Magnitude of wavefront distortions

4.1. *Basic distortion characteristics*

A volume of density field of size approximately 6.7δ in the streamwise direction, 2.9δ in the wall-normal direction and 2.3δ in the spanwise direction is saved every 4 time steps in the LES. Optical calculations are performed using these density-field data with the same grid resolution as the LES. An optical beam with an aperture size $6.7\delta \times 2.3\delta$ is shot from the wall in the normal direction. Snapshots of instantaneous wavefront distortions for the three Reynolds numbers are plotted in figure 5. They show that the wavefront distortions occur over a wide range of scales. Structures of increasingly smaller scales appear in the distorted wavefront as Reynolds number increases.

The time-averaged OPD_{rms} is found to be $8.87 \times 10^{-7}\delta$ for $Re_\theta = 875$, $6.82 \times 10^{-7}\delta$ for $Re_\theta = 1770$ and $5.59 \times 10^{-7}\delta$ for $Re_\theta = 3550$, which indicates that OPD_{rms} decreases with increasing Reynolds number. To investigate the influence of aperture size on OPD_{rms}, the two dimensions of the aperture are varied independently: first, the aperture size in the spanwise direction is fixed at 2.3δ while it is varied in the streamwise direction from 0.6δ to 6.7δ; second, the aperture size in the streamwise direction is fixed at 6.7δ while it is varied in the spanwise direction from 0.2δ to 2.3δ. The results are plotted in figure 6. It shows that OPD_{rms} increases with aperture size but the growth rate decreases. Owing to limitations in storage and computational time, it is not feasible to employ a sufficiently large aperture to allow the OPD_{rms} to fully saturate with respect to the aperture size. However, figure 6 shows a clear trend toward convergence for large aperture sizes, particularly in the spanwise direction. It
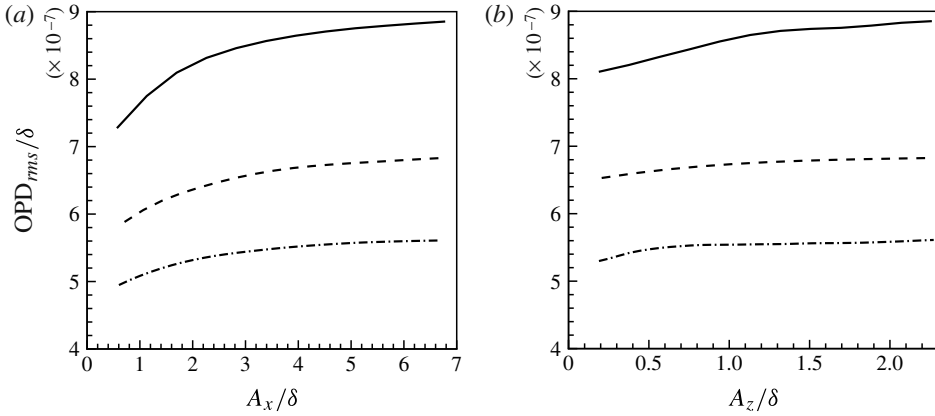
FIGURE 6. OPD$_{rms}$ as a function of (*a*) streamwise aperture size and (*b*) spanwise aperture size. ——, $Re_\theta = 875$; - - - -, $Re_\theta = 1770$; $-\cdot-$, $Re_\theta = 3550$.

also shows that OPD$_{rms}$ converges faster at high Reynolds numbers both in streamwise and spanwise directions due to reduced correlation length scales. The aperture size required for OPD$_{rms}$ saturation appears to be larger than the correlation lengths of the underlying index-of-refraction field, or the optical wavefront; see §5.1. It should be noted that the aperture size effect shown in figure 6 is based on tilt-removed OPD data. The unsteady tilt removal can affect the variation of OPD$_{rms}$ with the aperture size as demonstrated by Cress (2010). In fact, tilt removal acts as a simulated adaptive optical correction applied to the beam. Calculations without unsteady tilt removal indicate that OPD$_{rms}$ does not saturate with respect to the streamwise aperture size due to the growth of the boundary-layer thickness.

The effects of aperture size and Reynolds number on the streamwise tilt are illustrated in figure 7, where the vertical coordinate, *x-tilt*, represents the coefficient A in (2.15). The unsteady tilt decreases significantly with increasing Reynolds number and aperture size. Hence, the tilt removal as described in §2.2 affects a small-aperture beam in low-Reynolds-number flows much more significantly than a large-aperture beam in high-Reynolds-number flows.

The decreasing OPD$_{rms}$ with increasing Reynolds number is qualitatively supported by experimental results. Based on boundary-layer aero-optical measurements at high Reynolds numbers and the strong Reynolds analogy, Wyckham & Smits (2009) proposed the following scaling law for OPD$_{rms}$:

$$\text{OPD}_{rms} = C_w K_{GD} \rho_\infty \delta M_\infty^2 \sqrt{C_f} r_2^{-3/2}, \tag{4.1}$$

where $r_2 = 1 + [(\gamma - 1)/2]M_\infty^2[1 - r(U_c/U_\infty)^2]$ for adiabatic walls and $r_2 = (1/2)(T_w/T_\infty + 1)$ for isothermal walls, $r(\approx 0.9)$ is the recovery factor, T_w is the temperature of the wall, and C_w is a constant independent of Reynolds number and Mach number. Equation (4.1) clearly shows a Reynolds-number dependence through the skin friction coefficient C_f, indicating that OPD$_{rms}$ decreases with Reynolds number. This scaling law is based on experiments for hypersonic flows at Mach number $M = 7.6 \sim 7.8$ and Reynolds number $Re_\theta \approx 20\,000$, and subsonic flows at $M = 0.75 \sim 0.79$ and $Re_\theta \approx 10\,000$. More recently, Gordeyev *et al.* (2011) obtained the same C_f scaling of OPD$_{rms}$ based on the linking equation (Sutton 1985) and experimental measurements at $M = 2$ and $Re_\theta \approx 69\,000$. The OPD$_{rms}$ computed from
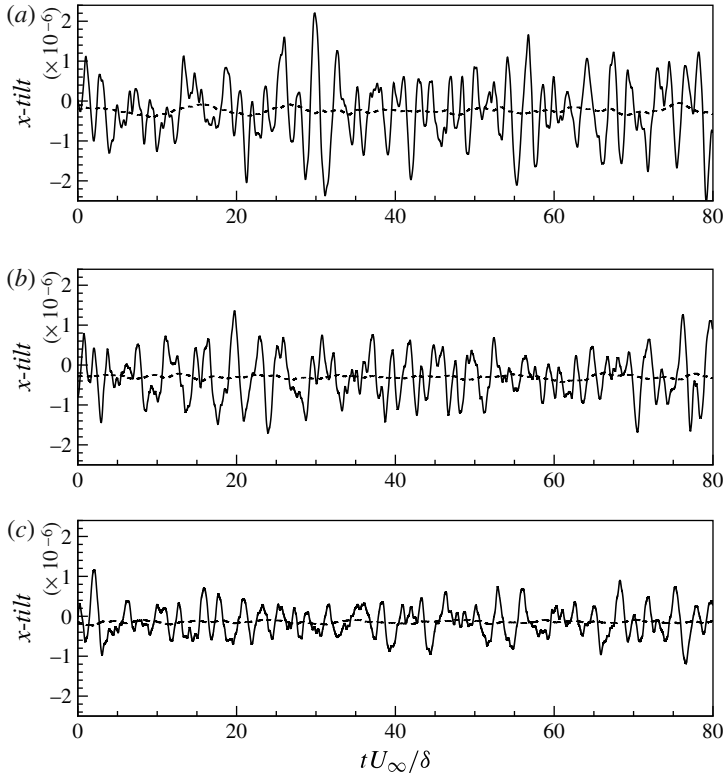
FIGURE 7. Streamwise tilt as a function of time at (*a*) $Re_\theta = 875$, (*b*) $Re_\theta = 1770$, and (*c*) $Re_\theta = 3550$ with two different streamwise aperture sizes: ——, $A_x = 1.1\delta$; - - - -, $A_x = 6.6\delta$.

LES data at the three Reynolds numbers is plotted in figure 8 along with a curve proportional to $\sqrt{C_f}$ with the coefficient in (4.1) adjusted arbitrarily to match the computed OPD$_{rms}$ at the intermediate Reynolds number. Discrepancies can be observed between the two curves, especially at the low-Reynolds-number end, indicating that the scaling law is not accurate for low-Reynolds-number flows. On the other hand, the figure shows that the difference decreases as Reynolds number increases. Since C_f varies slowly at high Reynolds numbers, it can be expected that wavefront distortions are relatively insensitive to Reynolds number for high-Reynolds-number flows. Numerical simulations at higher Reynolds numbers and/or experiments at lower Reynolds numbers are needed to fill the gap and further clarify the Reynolds-number dependence issue.

Given the near-field optical distortion magnitude, the optical system performance is often characterized in terms of the Strehl ratio, defined as the ratio of the maximum irradiance for an aberrated beam in the far field, $I(t)$, to the diffraction-limited on-axis irradiance, I_0. The time-averaged Strehl ratio is related to the time-averaged OPD$_{rms}$ by (Mahajan 1983)

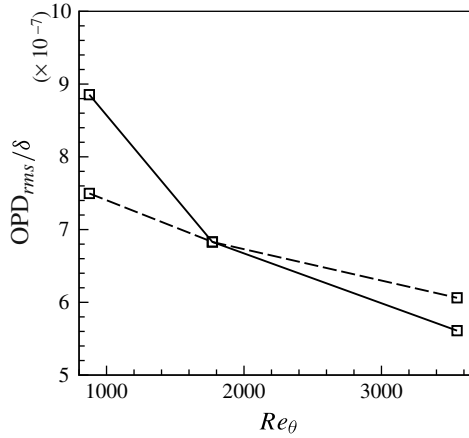$$\text{SR} = \frac{\bar{I}}{I_0} = \exp\left[-\left(\frac{2\pi \text{OPD}_{rms}}{\lambda}\right)^2\right]. \qquad (4.2)$$

FIGURE 8. OPD$_{rms}$ as a function of Reynolds number. ——, LES; ----, $1.11 \times 10^{-5}\sqrt{C_f}$.

Re_θ	875		1770		3550	
δ (cm)	2.5	5.0	2.5	5.0	2.5	5.0
OPD$_{rms}/\delta \times 10^7$	8.87	8.87	6.82	6.82	5.59	5.59
OPD$_{rms}/\lambda \times 10^2$	4.44	8.87	3.41	6.82	2.80	5.59
SR (%)	92.5	73.3	95.5	83.2	97.0	88.4

TABLE 2. Strehl ratio at different Reynolds numbers and boundary layer thicknesses for $\lambda = 0.5\ \mu m$.

As an example, suppose that the wavelength of a visible laser beam is 0.5 μm and the boundary-layer thickness is 2.5 and 5.0 cm for all the three Reynolds numbers, based on the LES data, then the estimated Strehl ratios are given in table 2. It can be noticed that for this laser beam, the low-Reynolds-number turbulent boundary layer of thickness 5.0 cm causes a system-performance reduction by as much as 27 %, while the performance degradation decreases with increasing Reynolds number. Under flight conditions, the Reynolds number is much higher than those in the current study and a performance reduction of less than 10 % can be expected at the same Mach number. However, due to the M^2 scaling of OPD$_{rms}$, the flight Mach number has a stronger effect on the system performance than the Reynolds number.

4.2. *Contribution from different flow regions*

To investigate contributions to wavefront distortions from different flow regions in the boundary layer, (2.11) is integrated from the wall to different y-locations, and the resulting OPD$_{rms}$ values are shown in figure 9. The results show that the viscous sublayer has little effect on the wavefront distortions. For all the cases, the distortions start to grow in the buffer layer, and most of the growth takes place in the logarithmic layer ($30 < y^+ < 110$ for $Re_\theta = 875$, $30 < y^+ < 160$ for $Re_\theta = 1770$ and $30 < y^+ < 250$ for $Re_\theta = 3550$) and wake region ($y^+ > 110$ for $Re_\theta = 875$, $y^+ > 160$ for $Re_\theta = 1770$ and $y^+ > 250$ for $Re_\theta = 3550$). The percentages of the OPD$_{rms}$ and the mean-square of OPD (OPD$_{ms}$) caused by different flow regions for the three Reynolds numbers are
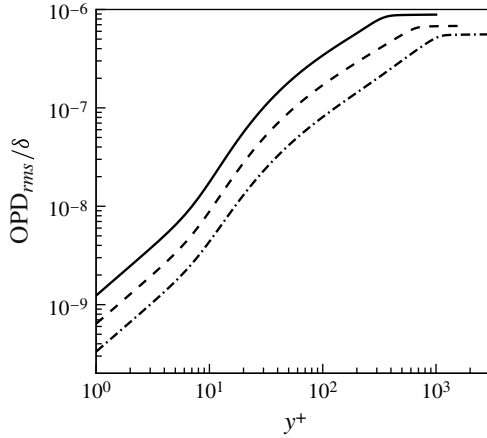
FIGURE 9. OPD_{rms} at different wall-normal locations. ——, $Re_\theta = 875$; - - - -, $Re_\theta = 1770$; $-\cdot-$, $Re_\theta = 3550$.

Re_θ	OPD_{rms}			OPD_{ms}		
	875	1770	3550	875	1770	3550
Viscous sublayer and buffer layer	11.34	7.20	4.09	1.29	0.52	0.17
Log layer	30.16	28.92	26.47	15.93	12.52	9.17
Wake region	58.50	63.88	69.44	82.78	86.96	90.66

TABLE 3. Percentages of OPD_{rms} and OPD_{ms} caused by different flow regions.

listed in table 3. Clearly, the wake region is the dominant contributor to the overall OPD for all three cases. The contribution from the viscous sublayer and buffer layer ($0 < y^+ < 30$) is approximately 11.34 % of the total distortion magnitude (OPD_{rms}) and 1.29 % of the total distortion energy (OPD_{ms}) for the lowest Reynolds number, and this ratio decreases with increasing Reynolds number. At $Re_\theta = 3550$, only approximately 4.09 % of the distortion magnitude and 0.17 % of the distortion energy come from the viscous sublayer and buffer layer, while the wake-region contributions increase to more than 69 % of the distortion magnitude and more than 90 % of the distortion energy. It can be expected that when the Reynolds number is sufficiently large, the contribution from the viscous sublayer and buffer layer will become negligible. More discussions of the optical importance of different flow regions in the context of the linking equation will follow in § 6 (see figure 21).

In practical aero-optical problems involving optical turrets at flight conditions, the Reynolds number is very high (of the order of 10^6 based on the turret size and free-stream velocity and 10^5 based on the attached boundary-layer thickness (Gordeyev & Jumper 2010)). It is not feasible to perform LES which resolves energetic flow scales down to the wall. Instead, a hybrid RANS/LES method or LES with a wall-layer model is required. In LES with a wall model, the first off-wall grid point is generally in the log layer, and its applicability for aero-optical prediction depends on the relative contribution from the near-wall region. The present results illustrate that wavefront distortions are predominantly caused by the wake region, and the relative contribution
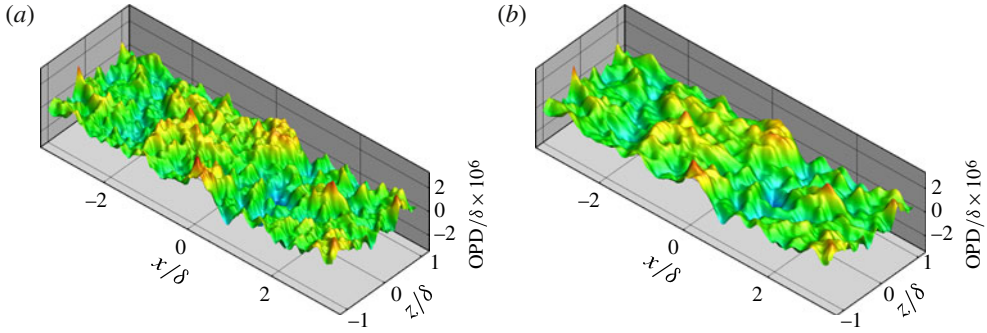
FIGURE 10. Instantaneous OPD obtained with filtered density fields. (*a*) filter width = 4 grid spacings; (*b*) filter width = 8 grid spacings.

from the viscous sublayer and buffer layer decreases with increasing Reynolds number. This suggests that for high-Reynolds-number flows LES with wall modelling can be an accurate and efficient technique for aero-optical applications.

4.3. *Effect of turbulence scales*

The effect of small-scale turbulence on wavefront distortions is of practical importance for both computational and experimental studies of aero-optics, as it determines the grid resolution required for computations and the spatial resolution requirement for wavefront sensors. It is generally understood from previous investigations (Mani *et al.* 2008, 2009) that small-scale contributions to OPD_{rms} are relatively small, and DNS-type resolution is not required. In this section, the role of small scales in turbulent boundary layers is examined in terms of not only OPD_{rms} but also the frequency spectra of OPD.

To study the small-scale effect, spatial filters of progressively larger filter widths are used to filter the density field obtained from LES at the highest Reynolds number $Re_\theta = 3550$. The filter is of top-hat type in physical space and is implemented numerically using Simpson's rule. Optical calculations are then performed with the filtered density field. The filter width varied from 2 grid spacings to 4 and then 8 grid spacings in streamwise and spanwise directions to filter out turbulence structures at different scales. Based on grid spacings of $\Delta x/\delta = 0.025$ in the streamwise direction and $\Delta z/\delta = 0.008$ in the spanwise direction for $Re_\theta = 3550$, the three filter widths in physical units are given in table 4.

Instantaneous wavefront distortions computed from the filtered density field with filter width of 4 and 8 grid spacings are shown in figure 10. The original wavefront distortions calculated from the unfiltered density field at the same time instant can be found in figure 5(*c*). From these results, it can be observed that filtering smoothed out the wavefront distortions by removing the small scales, and larger filter widths resulted in smoother OPD variations.

The OPD_{rms} computed from the filtered density fields with different filter widths is plotted in figure 11 as a function of wall-normal distance. It shows that filtering the density field with filter widths of 2 and 4 grid spacings causes less than 5 % reduction in OPD_{rms}, whereas the filter with a width of 8 grid spacings reduces OPD_{rms} by 11 %.

The effect of filtering on the power spectral density of OPD at the streamwise location of the beam centre as a function of frequency is illustrated in figure 12. The
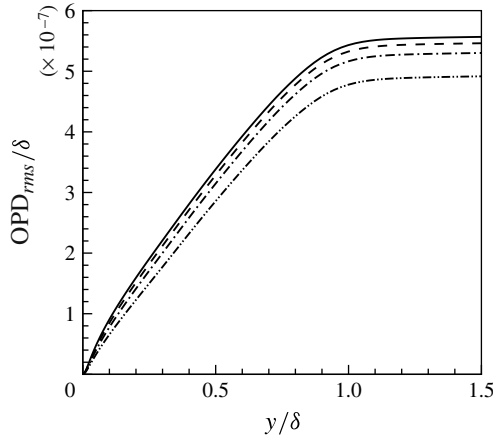
FIGURE 11. Comparison of OPD_{rms} obtained from filtered density fields with different filter widths for $Re_\theta = 3550$. ——, unfiltered; - - - -, 2 grid spacings; $-\cdot-$, 4 grid spacings; $-\cdot\cdot-$, 8 grid spacings.
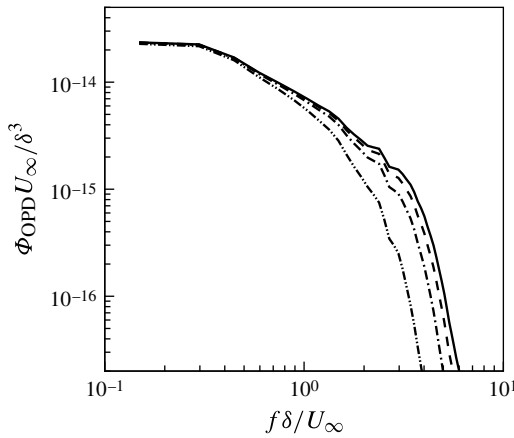

FIGURE 12. Frequency spectra of OPD obtained from filtered density fields with different filter widths for $Re_\theta = 3550$. ——, unfiltered; - - - -, 2 grid spacings; $-\cdot-$, 4 grid spacings; $-\cdot\cdot-$, 8 grid spacings.

Filter width	2 grid spacings		4 grid spacings		8 grid spacings	
	Δ_x/δ	Δ_z/δ	Δ_x/δ	Δ_z/δ	Δ_x/δ	Δ_z/δ
$Re_\theta = 3550$	0.050	0.016	0.100	0.032	0.200	0.064

TABLE 4. Filter widths in physical units.

power spectral density is defined as

$$\Phi_{OPD}(x, f) = \int_{-\infty}^{+\infty} \overline{\langle OPD(x, z, t) OPD(x, z, t + \Delta t) \rangle} e^{-2\pi i f \Delta t} \, d\Delta t, \qquad (4.3)$$
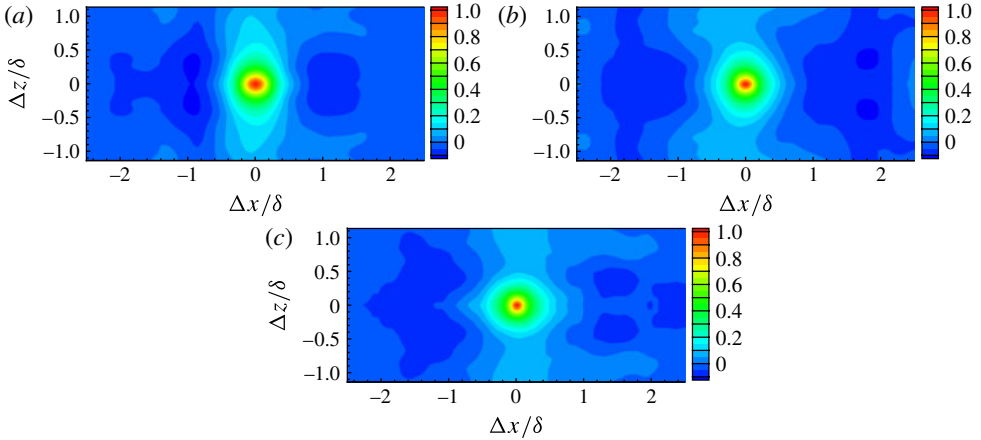
FIGURE 13. Two-point spatial correlations of OPD with origin at the beam centre for three Reynolds numbers: (a) $Re_\theta = 875$; (b) $Re_\theta = 1770$; (c) $Re_\theta = 3550$.

where the angle brackets and overbar denote spanwise and time averages, respectively. It shows that, as expected, filtering removes primarily the high-frequency content of OPD which corresponds to small-scale turbulence; the low-frequency end of the spectrum is essentially intact. The filtering effect is not significant until the filter width is as large as 8 grid spacings. The findings in this section indicate that small-scale turbulence structures are relatively inactive from an optical standpoint, and wavefront distortions are predominantly caused by the energetic, coherent large-scale structures. This observation is consistent with the findings by Truman (1992), Zubair & Catrakis (2007) and Mani et al. (2008) for other types of turbulent flows.

5. Structure of wavefront distortions

5.1. Two-point correlations of OPD

In this section, the two-point spatial correlations of OPD are examined to reveal the structure of wavefront distortions and its dependence on Reynolds number. The two-point spatial correlation of OPD can be computed from

$$R_{OPD}(x, \Delta x, \Delta z) = \frac{\overline{\langle OPD(x, z, t) OPD(x + \Delta x, z + \Delta z, t)\rangle}}{\sqrt{\overline{\langle OPD^2(x)\rangle}}\sqrt{\overline{\langle OPD^2(x + \Delta x, \Delta z)\rangle}}}. \tag{5.1}$$

Iso-contours of OPD two-point correlations are shown in figure 13 with the origin at the centre of aperture. The correlation function is independent of the origins in z and t because the turbulent flow is homogeneous in the spanwise direction and stationary in time. The nearly symmetric shapes of the correlations with respect to $\Delta x = 0$ suggests that the streamwise inhomogeneity is weak. It is noted that the shape of the correlation contours changes with Reynolds number. At $Re_\theta = 875$, OPD has a shorter correlation length in the streamwise direction than in the spanwise direction. As the Reynolds number increases, the correlation length increases in the streamwise direction but decreases in the spanwise direction. At $Re_\theta = 1770$, the correlation contours are nearly isotropic while at $Re_\theta = 3550$, the correlation length in the streamwise direction exceeds that in the spanwise direction. With this trend, it appears likely that at even higher Reynolds numbers, the correlation contours will be
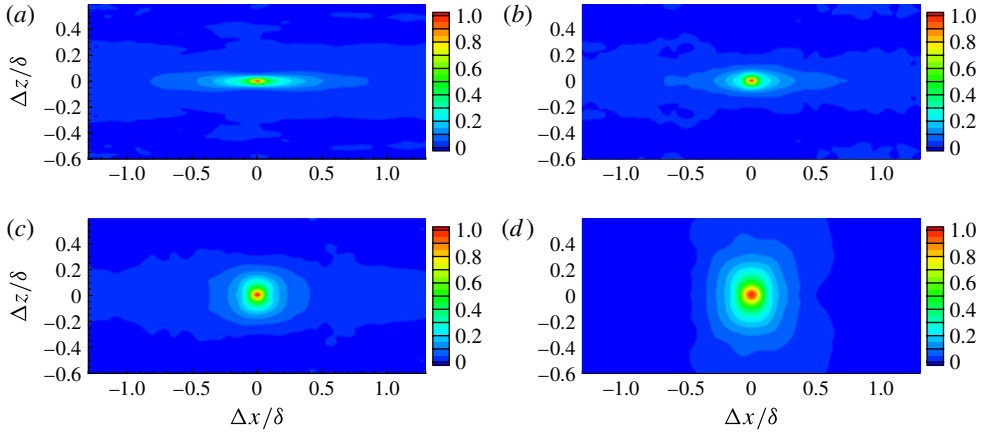
FIGURE 14. Two-point spatial correlations of density fluctuations in four x–z planes with origin at the beam centre, at $Re_\theta = 3550$: (*a*) $y^+ = 10$; (*b*) $y^+ = 50$; (*c*) $y^+ = 198$; (*d*) $y^+ = 807$.

elongated in the streamwise direction. This observation agrees qualitatively with the findings of Wittich *et al.* (2007) who used a Malley probe and Taylor's hypothesis to obtain spatial correlations of OPD. They reported that the streamwise correlation length is six times longer than the spanwise one at $Re_\theta \approx 26\,000$. On the other hand, with a two-dimensional wavefront sensor, Wyckham & Smits (2009) observed nearly isotropic two-point correlations of OPD induced by subsonic boundary layers at $Re_\theta \approx 10\,000$. It should be noted that the aperture size employed by Wyckham & Smits (2009) is approximately $2\delta \times 2\delta$, which is much smaller than the aperture size $6.7\delta \times 2.3\delta$ employed in the current study. Owing to the unsteady tilt removal, correlation lengths are affected by the aperture size employed (Cress 2010), which can be partly responsible for the differences in the two-point spatial correlations of OPD.

The shape of OPD correlation contours is determined by the structure of density fluctuations. Figure 14 shows two-point spatial correlations of fluctuating density in four x–z planes with the origin at the beam centre for the case of $Re_\theta = 3550$. It is noted that the shape of correlation contours changes drastically from bottom to top of the boundary layer. In the buffer layer (figure 14*a*), the correlation contours are elongated in the streamwise direction and very narrow in the spanwise direction, reflecting the near-wall streaky structures (hairpin vortex legs). These structures can be seen clearly in the instantaneous density field (figure 15*a*) and the associated OPD contours (figure 15*b*) at the same *y*-location. The correlation lengths in the two directions become comparable in the upper log layer (figure 14*c*) and, eventually in the wake region, the spanwise correlation length becomes larger than the streamwise one (figure 14*d*). By comparing the shapes of correlation contours for OPD (figure 13*c*) and fluctuating density (figure 14, note difference in plotted spatial scales), it is evident that the spatial correlation of OPD is unlike the spatial correlation of density fluctuations in any single x–z plane; it is an integrated effect of turbulence structures across the entire boundary-layer thickness. The two-point spatial correlations of density fluctuations and OPD for the two lower-Reynolds-number cases have also been examined, and the same qualitative relations have been observed.
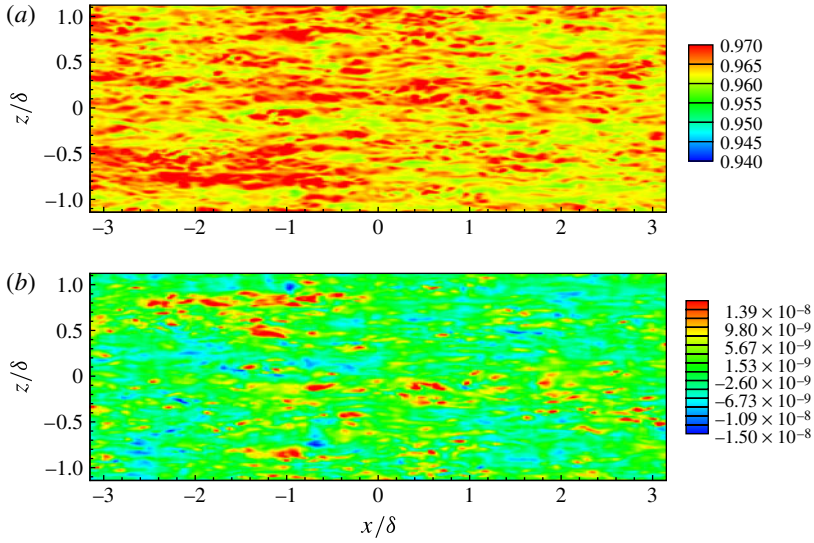
FIGURE 15. (a) Instantaneous density field ρ/ρ_∞ and (b) corresponding OPD/δ in the x–z plane with the origin at the beam centre at $y^+ = 10$ for $Re_\theta = 3550$.

5.2. *Space–time correlations of OPD*

The space–time correlation of OPD as a function of streamwise spatial and temporal separations can be calculated from

$$R_{OPD}(\Delta x, \Delta t; x) = \frac{\overline{\langle \text{OPD}(x,t)\text{OPD}(x+\Delta x, t+\Delta t)\rangle}}{\sqrt{\langle \text{OPD}^2(x)\rangle}\sqrt{\langle \text{OPD}^2(x+\Delta x)\rangle}}. \tag{5.2}$$

Iso-contours of space–time correlations of OPD at the centre of the aperture for the case of $Re_\theta = 3550$ are plotted in figure 16. The contours are similar to those for wall-pressure fluctuations underneath a turbulent boundary layer and demonstrate dominance by convection. From these correlations the convection velocities of OPD as a function of temporal separation or spatial separation can be computed from (Choi & Moin 1990):

$$U_c(\Delta t) = \frac{\Delta x_c}{\Delta t}, \quad \left.\frac{\partial R_{OPD}(\Delta x, \Delta t)}{\partial \Delta x}\right|_{\Delta x = \Delta x_c} = 0, \tag{5.3}$$

$$U_c(\Delta x) = \frac{\Delta x}{\Delta t_c}, \quad \left.\frac{\partial R_{OPD}(\Delta x, \Delta t)}{\partial \Delta t}\right|_{\Delta t = \Delta t_c} = 0. \tag{5.4}$$

The convection velocities are important parameters for aero-optical analysis based on Malley probe data (Jumper & Fitzgerald 2001).

The convection velocities for the three Reynolds numbers are shown in figure 17. They are approximately $0.8U_\infty$ at the small temporal separation of $\Delta t \approx 0.05\delta/U_\infty$ and $0.84U_\infty$ at the small spatial separation of $\Delta x \approx 0.06\delta$ for all three Reynolds numbers. The convection velocity for small spatial separations agrees well with that measured experimentally by Buckner *et al.* (2005), who reported a value of $0.81U_\infty$ for a separation of 0.05δ.

The convection velocity for OPD increases with increasing temporal and spatial separations since the larger flow structures responsible for optical distortions at these
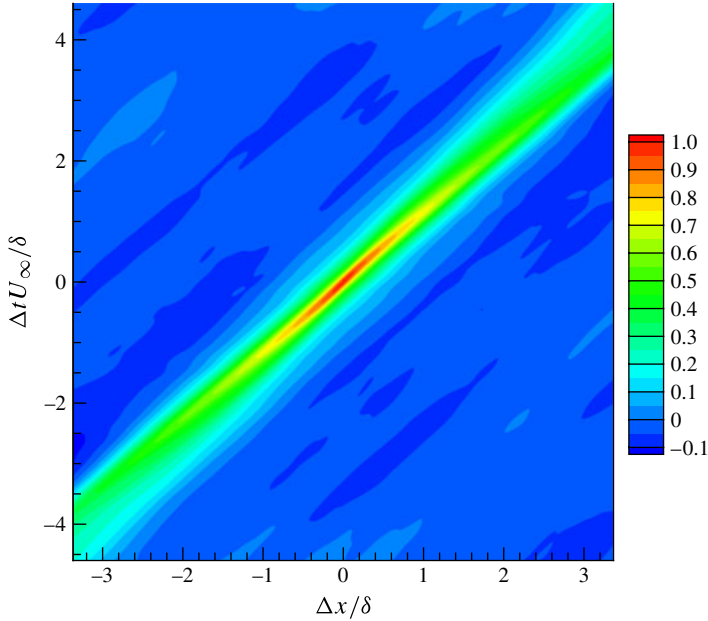
FIGURE 16. Space–time correlations of OPD for $Re_\theta = 3550$ as a function of streamwise spatial and temporal separations, with origin at the centre of the aperture.
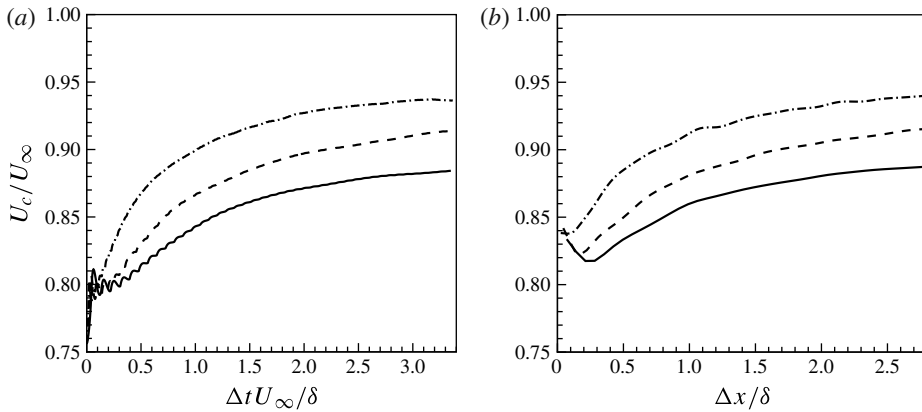

FIGURE 17. Convection velocities of OPD as a function of (*a*) temporal separation, and (*b*) streamwise spatial separation. ——, $Re_\theta = 875$; - - - -, $Re_\theta = 1770$; – · –, $Re_\theta = 3550$.

scales reside in the outer layer and therefore travel faster. At a temporal separation of $3.3\delta/U_\infty$ or a spatial separation of 2.8δ, the convection velocities reach approximately $0.87U_\infty$ for $Re_\theta = 875$ and $0.93U_\infty$ for $Re_\theta = 3550$. The variation of convection velocities for OPD from small to large separations is significantly smaller than that for wall-pressure fluctuations (Choi & Moin 1990). This is because the OPD convection velocity is predominantly determined by the outer region of the boundary layer, whereas in the case of wall-pressure fluctuations, small eddies in the near-wall region, which have lower convection velocities, contribute directly to small-scale wall-pressure fluctuations.

At large temporal or spatial separations, the convection velocities increase with Reynolds number. This again shows dominance of the outer region of the boundary layer which grows in size relative to the inner layer as Reynolds number increases. As demonstrated in § 4.2, the relative contribution of the log layer and wake region to OPD_{rms} increases with Reynolds number.

6. The linking equation

In aero-optics, the linking equation derived by Sutton (1985) is widely used to relate wavefront-distortion statistics to statistics of the aberrating flow field:

$$\overline{\langle \phi^2 \rangle} = 2K_{GD}^2 k^2 \int_0^L \overline{\langle \rho'^2 \rangle} \Lambda(y)\, dy, \qquad (6.1)$$

where $\overline{\langle \phi^2 \rangle} = 4\pi^2 \overline{\langle OPD^2 \rangle}/\lambda^2$ is the wavefront phase distortion, Λ is the correlation length of the fluctuating density field in the direction of propagation, and $k = 2\pi/\lambda$ is the optical wavenumber. This equation was derived for locally homogeneous turbulence (statistics do not vary greatly over a correlation length) with a Gaussian temporal distribution, and its applicability to inhomogeneous turbulent flows has been questioned. A more general form of the linking equation takes the form (Steinmetz 1982; Havener 1992)

$$\overline{\langle \phi^2 \rangle} = K_{GD}^2 k^2 \int_0^L \int_0^L R_{\rho\rho}(y, y')\, dy'\, dy, \qquad (6.2)$$

where $R_{\rho\rho}(y, y')$ is the two-point density correlation along the optical path. Equation (6.2) can also be derived following an earlier analysis of Liepmann (1952) for the mean-square deflection angle of a small aperture beam coupled with Taylor's hypothesis (Jumper & Fitzgerald 2001).

Based on LES data, Tromeur *et al.* (2006*a*,*b*) evaluated Sutton's linking equation (6.1) for a Mach 0.9 turbulent boundary layer and noticed large discrepancies between the results obtained by directly integrating the index-of-refraction field, (2.11) and (2.13), and by using Sutton's linking equation, (6.1). Consequently, they questioned the applicability of Sutton's model to boundary-layer flows and suggested that results could be improved by using the velocity integral scale instead of the density integral scale in the model. Hugo & Jumper (2000) examined the applicability of Sutton's linking equation to a heated two-dimensional jet using density correlations obtained from hot-wire measurements. They found that the oscillatory nature of the correlation coefficient in the shear-layer regions made the evaluation of the length scale difficult. It was concluded that if the length scale was based on integrating the correlation coefficient between the first zero-crossings at negative and positive separations, Sutton's equation gave reasonable results.

The equilibrium turbulent boundary layers considered here are homogeneous in the spanwise direction, vary slowly in the streamwise direction, and are highly inhomogeneous in the wall-normal direction. In this section, the validity and accuracy of the linking equation for boundary-layer flows are evaluated using the simulation data. The derivation leading to Sutton's linking equation and the underlying assumptions are examined first, and the appropriate form of the correlation length in (6.1) is identified for accurate aero-optical predictions of boundary-layer flows.

To facilitate the analysis, the density is decomposed as $\rho(x, y, z, t) = \rho_0(y) + \rho'(x, y, z, t)$, where $\rho_0(y) = \overline{\langle \rho(x, y, z, t) \rangle}$ is the density averaged in time and over the x–z plane, and ρ' is the density fluctuation relative to the mean. Based on (2.12), the

optical index of refraction can then be expressed as $n(x, y, z, t) = n_0(y) + n'(x, y, z, t)$, with $n_0 = 1 + K_{GD}\rho_0$ and $n' = K_{GD}\rho'$. Substituting this decomposition into (2.11) and (2.13) leads to

$$\text{OPD}(x, z, t) = \int_0^L n'(x, y, z, t)\,\mathrm{d}y - \int_0^L \langle n'(x, y, z, t)\rangle\,\mathrm{d}y. \tag{6.3}$$

Consequently, the time average of the OPD mean-square in the aperture plane is

$$\overline{\langle \text{OPD}^2\rangle} = \overline{\left\langle \left[\int_0^L n'(x, y, z, t)\,\mathrm{d}y\right]^2 \right\rangle} - \overline{\left[\int_0^L \langle n'(x, y, z, t)\rangle\,\mathrm{d}y\right]^2}. \tag{6.4}$$

If turbulence is assumed homogeneous in both x- and z-directions, and the aperture size is much larger than the correlation length, then $\langle n'\rangle \approx 0$, and (6.4) takes the form

$$\overline{\langle \text{OPD}^2\rangle} = K_{GD}^2 \int_0^L \int_0^L \overline{\langle \rho'(x, y, z, t)\rho'(x, y', z, t)\rangle}\,\mathrm{d}y'\,\mathrm{d}y \tag{6.5}$$

upon substitution of $n' = K_{GD}\rho'$. This is the general form of the linking equation (6.2). With a change of variable $\Delta y = y' - y$, (6.5) becomes

$$\overline{\langle \text{OPD}^2\rangle} = K_{GD}^2 \int_0^L \int_{-y}^{L-y} \overline{\langle \rho'(x, y, z, t)\rho'(x, y + \Delta y, z, t)\rangle}\,\mathrm{d}\Delta y\,\mathrm{d}y. \tag{6.6}$$

By defining

$$R_{\rho\rho}(y, \Delta y) = \frac{\overline{\langle \rho'(x, y, z, t)\rho'(x, y + \Delta y, z, t)\rangle}}{\overline{\langle \rho'^2(x, y, z, t)\rangle}} \tag{6.7}$$

and

$$\Lambda(y) = \frac{1}{2}\int_{-y}^{L-y} R_{\rho\rho}(y, \Delta y)\,\mathrm{d}\Delta y, \tag{6.8}$$

(6.6) becomes the same as Sutton's linking equation (6.1).

The above results illustrate that the general form of the linking equation is valid for large-aperture beams through turbulent flows which are statistically homogeneous in directions parallel to the aperture. There is no restriction imposed in the direction of optical propagation. Sutton's original linking equation (6.1) is formally more restrictive, requiring turbulence to be quasi-homogeneous in the direction of propagation. Nonetheless, it is still applicable for beams traversing strongly inhomogeneous turbulence, as in the case of a boundary layer, if the length scale Λ is defined according to (6.7) and (6.8). Note that the correlation coefficient $R_{\rho\rho}$ in (6.7) is based on the definition for homogeneous turbulence. The standard definition for inhomogeneous turbulence

$$R_{\rho\rho}(y, \Delta y) = \frac{\overline{\langle \rho'(x, y, z, t)\rho'(x, y + \Delta y, z, t)\rangle}}{\sqrt{\overline{\langle \rho'^2(x, y, z, t)\rangle}}\sqrt{\overline{\langle \rho'^2(x, y + \Delta y, z, t)\rangle}}} \tag{6.9}$$

will not lead to Sutton's equation. Furthermore, the integration bounds in (6.8) are not from $-\infty$ to ∞ as in the standard definition; they must be modified to accommodate the finite thickness of the aberrating field.

Figure 18 shows the density correlation function calculated using (6.7) in the wall-normal direction at four different wall-normal locations for $Re_\theta = 3550$. The density
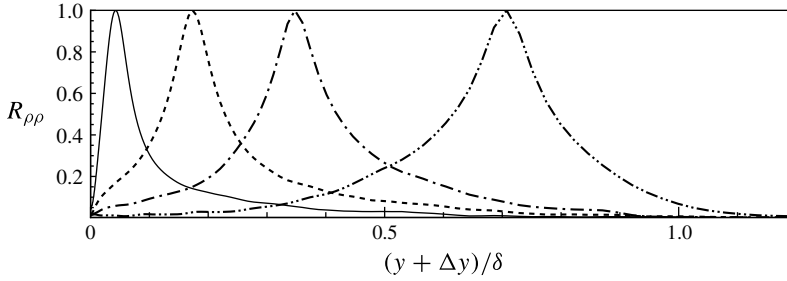
FIGURE 18. Density correlation function defined in (6.7) with origin at four wall-normal locations along the beam centreline for $Re_\theta = 3550$. ——, $y^+ = 50$; - - - -, $y^+ = 198$; $-\cdot-$, $y^+ = 396$; $-\cdot\cdot-$, $y^+ = 807$.
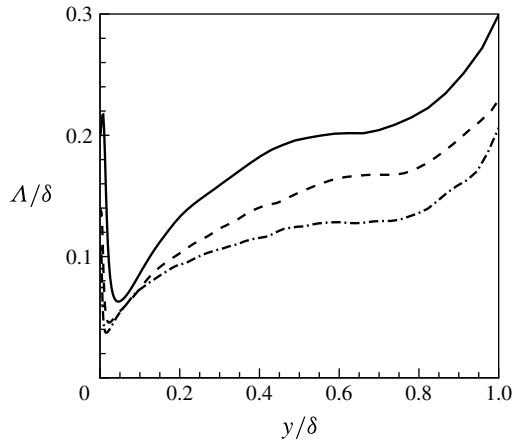

FIGURE 19. Density correlation length as a function of wall-normal locations calculated using (6.7) and (6.8) for three Reynolds numbers: ——, $Re_\theta = 875$; - - - -, $Re_\theta = 1770$; $-\cdot-$, $Re_\theta = 3550$.

correlation length calculated from (6.8) is plotted in figure 19 for all three Reynolds numbers as a function of wall-normal locations. It can be noticed that the correlation length increases from the near-wall region to the edge of the boundary layer. At the same wall-normal location, the correlation length decreases with increasing Reynolds number. Based on these results, Sutton's linking equation is used to estimate OPD_{rms} and the results are shown in figure 20 together with the OPD_{rms} calculated by direct integration of the index-of-refraction field. Sutton's linking equation with the correlation length defined in (6.8) shows very good agreement with the directly integrated values. This is because the approximations involved in the derivation of the linking equation, namely the large aperture size and statistical homogeneity in the streamwise and spanwise directions, are largely satisfied. The weak inhomogeneity in the streamwise direction is mainly responsible for the small discrepancies observed.

The derivation of the linking equation for boundary-layer flows and the agreement between the results from the linking equation and direct integration confirm the comments by Hugo & Jumper (2000) that Sutton's linking equation can be applied to inhomogeneous and anisotropic flows if the density length scales are 'appropriately' calculated. The key to the appropriate calculation is to use the correlation length
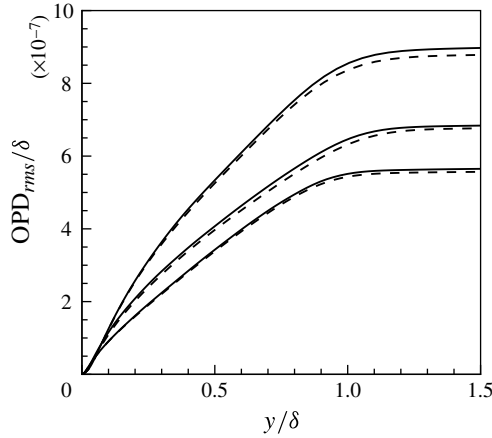
FIGURE 20. Comparison of OPD$_{rms}$ calculated by direct integration and Sutton's linking equation at three Reynolds numbers: ——, direct integration; - - - -, Sutton's linking equation. From top to bottom: $Re_\theta = 875$, 1770 and 3550.
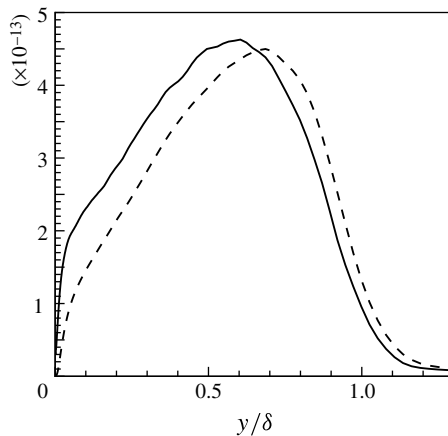

FIGURE 21. Contribution to $\overline{\langle OPD^2 \rangle}/\delta^2$ from unit length of the optical path across the boundary layer for $Re_\theta = 3550$: ——, calculated from $2K^2_{GD}\rho'_{ms}(y)\Lambda(y)$; - - - -, calculated from $\mathrm{d}OPD_{ms}/\mathrm{d}y$ based on directly integrated OPD.

defined by (6.8) along with the correlation function given by (6.7), or their reasonable approximations. An examination of Tromeur *et al.* (2006*a,b*) indicates that the poor prediction of Sutton's model in their calculation is caused by the use of a correlation length that is inconsistent with the derivation of Sutton's equation; their correlation length is twice that given by (6.8). Hugo & Jumper (2000) employed the correct correlation-length definition in their heated-jet investigation. The difficulty encountered by them is due to the oscillatory nature of the correlation function with large negative values and limited experimental data, which prevented an accurate evaluation of the correlation length according to the definition.

From the linking equation (6.1), since the integral of $2K^2_{GD}\rho'_{ms}(y)\Lambda(y)$ over the optical path is $\overline{\langle OPD^2 \rangle}$, the former quantity can be interpreted as the contribution to
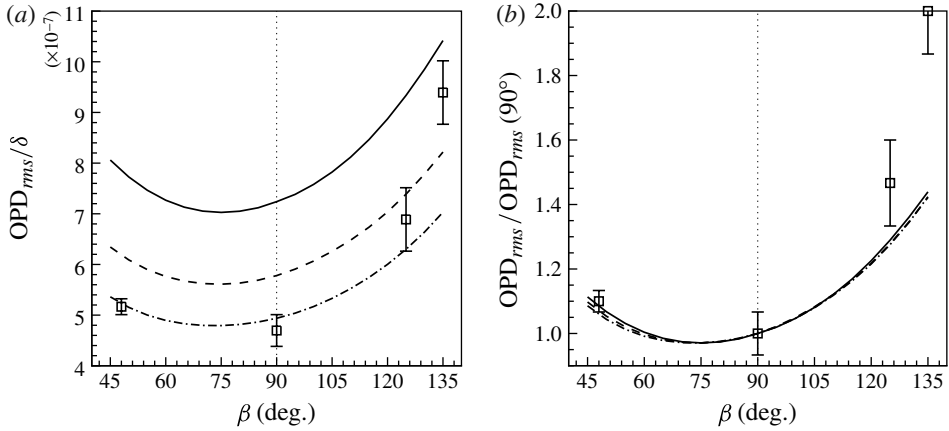
FIGURE 22. OPD$_{rms}$ as a function of beam elevation angle: (*a*) OPD$_{rms}/\delta$; (*b*) OPD$_{rms}$/OPD$_{rms}$(90°). ——, $Re_\theta = 875$; - - - -, $Re_\theta = 1770$; –·–, $Re_\theta = 3550$; □ with error bars, experimental data of Cress *et al.* (2008) for $Re_\theta \approx 28\,800$.

the overall $\overline{\langle OPD^2 \rangle}$ from unit distance of propagation along the optical path. Likewise, the inner integral in (6.6) times $2K_{GD}^2$ can also be interpreted as such. In figure 21 this 'aberration density' calculated from $2K_{GD}^2 \rho'_{ms}(y) \Lambda(y)$ is plotted as the solid line across the boundary layer, which clearly shows the relative optical importance of different positions in the boundary layer. Alternatively, the aberration density can be interpreted as the y-derivative of the $\overline{\langle OPD^2 \rangle}$ computed from direct integration, which is shown as the dashed line in the figure. Although the two curves differ quantitatively, they display a consistent trend and show that the peak contribution comes from the region 0.5δ–0.7δ from the wall. The result based on the linking equation shows increased contributions from the near-wall region at the expense of the outer region because it accounts for the effect of not only the density fluctuation level but also the correlation length, which is affected by the region above a given y-location.

7. Effect of elevation angle

In practical applications it is often required to shoot an optical beam through a turbulent boundary layer in directions other than normal to the wall. To investigate the directional dependence of wavefront distortions, beams with different elevation angles β are examined. The elevation angle is defined as the angle between the optical path and the upstream direction. For $\beta < 90°$, the beam is tilted towards the upstream direction, while for $\beta > 90°$ it is tilted towards the downstream direction. Given the limited computational domain size, to allow an investigation at elevation angles from $45°$ to $135°$, a small aperture of size 0.6δ in the streamwise direction and 2.3δ in the spanwise direction is adopted. All beams propagate to the same height of 2.9δ above the wall.

The values of OPD$_{rms}$ as a function of elevation angle are plotted in figure 22 for the three Reynolds numbers. In figure 22(*a*) the distortion magnitude is normalized by the local boundary-layer thickness. It is seen to be significantly dependent on the direction of propagation, and is asymmetric with respect to the normal angle $\beta = 90°$; a beam tilted toward downstream experiences more distortions than one that is tilted toward upstream at the same angle relative to the normal direction. The curves for

the three Reynolds numbers differ in magnitude but not the overall shape. When normalized by their respective values at 90°, the three curves nearly collapse as shown in figure 22(*b*), indicating that Reynolds number has little effect on the elevation-angle dependence of OPD.

The asymmetry of optical aberrations was noted earlier in the numerical investigation of Truman & Lee (1990), who studied phase distortions in an optical beam through a homogeneous turbulent flow with constant mean shear, based on DNS of incompressible flow with passive scalar transport. Sensitivity to propagation direction was shown in their results and explained in terms of the orientation of hairpin vortices. Similar phenomena were observed experimentally in boundary layers by Cress *et al.* (2008). Their experimental data, obtained for $Re_\theta \approx 28\,800$, are plotted in figure 22 along with the numerical results and show the same trend as the latter. Cress *et al.* (2008) also pointed out that the asymmetry is due to the well-known, highly anisotropic vortical structures in the boundary layer (Robinson 1991; Adrian 2007). In quantitative terms, the experimental results are close to the LES results at the highest Reynolds number. It should, however, be noted that there are some differences between the numerical and experimental conditions. On the one hand, the aperture size in the streamwise direction is 0.6δ in the current study, which is much smaller than the aperture size of 10δ employed in the experiment. As discussed in §4.1, a larger aperture size increases the value of OPD$_{rms}$. On the other hand, the Reynolds number in the numerical investigation is much lower than that in the experiment. A higher Reynolds number leads to smaller values of OPD$_{rms}$. Taking both factors into consideration, a reasonable agreement between LES and experimental values can be expected at the same conditions.

The directionality of the OPD is best explained based on the linking equation (6.1), which shows an explicit dependence of OPD on the density fluctuation magnitude, correlation length and distance of propagation. In the flat-plate boundary layer, both the propagation distance within the boundary layer and the correlation length contribute to the elevation-angle dependence, but the asymmetry with respect to the normal direction is predominantly due to the correlation-length difference since the growth in boundary-layer thickness is small within the β-angle range considered. The correlation length is longer along an optical path tilted toward the downstream direction than toward the upstream direction, because the former is more aligned with the oblique vortical structures whereas the latter traverses those structures. To illustrate this, the two-point spatial correlations of fluctuating density are depicted in figure 23 as a function of Δx and Δy at the streamwise location of the beam centre and three y-positions for $Re_\theta = 3550$. Strong anisotropy of the correlation contours, particularly at large spatial separations, are evident, and the characteristics of these structures vary across the boundary layer. The angular position of the maximum correlation length relative to the flow direction increases away from the wall, which is consistent with the orientation of hairpin vortices.

A more detailed description of the density correlation length as defined in (6.8) is shown in the polar diagram in figure 24 as a function of elevation angle at four wall-normal locations. It is observed that in the near-wall region, where the bottom portions of hairpin vortex legs reside, the fluctuating density has a large correlation length in both the upstream and downstream directions at shallow angles. Away from the wall, the correlation length in the downstream region is significantly longer than in the upstream region, which directly accounts for the larger optical aberrations for downstream-tilted beams. The angle of maximum correlation length decreases (increases if measured from downstream direction) with wall-normal distance and is
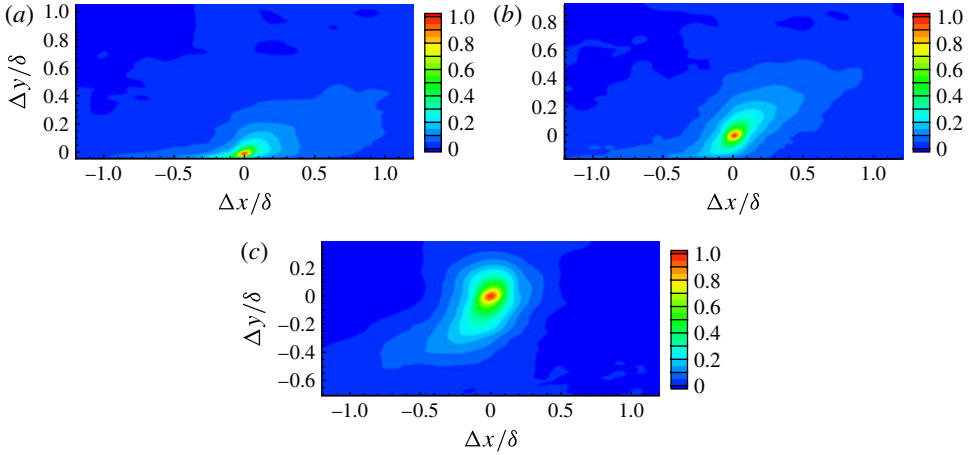
FIGURE 23. Two-point correlations of density fluctuations as a function of Δx and Δy at the streamwise location of the beam centre and three y-locations for $Re_\theta = 3550$: (*a*) $y^+ = 50$; (*b*) $y^+ = 198$; (*c*) $y^+ = 807$.
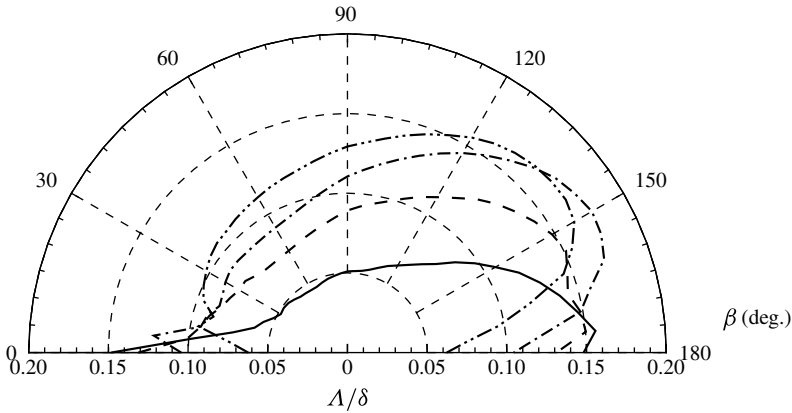

FIGURE 24. Density correlation length defined by (6.8) as a function of elevation angle for $Re_\theta = 3550$ at four y-locations: ——, $y^+ = 50$; - - - -, $y^+ = 198$; —·—, $y^+ = 396$; —··—, $y^+ = 807$.

approximately 135° (45° from the downstream wall) at $y^+ = 807$. These observations are again consistent with the well-known characteristics of coherent vortical structures in boundary layers.

8. Conclusion

Compressible large-eddy simulations have been performed to investigate the aero-optical effects of Mach 0.5 turbulent boundary layers at Reynolds numbers $Re_\theta = 875$, 1770 and 3550 based on the momentum thickness at the centre of the optical aperture. Highly resolved density-field data are obtained, from which the fluctuating index-of-refraction field is computed through the Gladstone–Dale relation, and wavefront distortions in terms of the optical path difference are calculated. The magnitude and structures of wavefront distortions are investigated, and their

dependence on Reynolds number, flow region, flow scale and elevation angle are examined. The physical mechanisms for optical distortions are analysed in terms of their relations with temperature and pressure fluctuations and turbulence structures in the boundary layer.

The results show that wavefront distortions are dependent on Reynolds number within the Reynolds-number range considered in the current numerical simulations. The OPD_{rms} is found to decrease with increasing Reynolds number, but the rate of decrease slows down as the Reynolds number increases, which suggests that wavefront distortions may be insensitive to Reynolds number for sufficiently high Reynolds numbers. Reynolds-number dependence is also observed in the spatial structure of OPD; the spanwise correlation length of OPD decreases with Reynolds number, whereas its streamwise correlation length increases with Reynolds number. An examination of the two-point correlations of density fluctuations in planes parallel to the wall demonstrates that OPD structures reflect the integrated effect of the fluctuating-density structures, which evolve from being streamwise elongated in the near-wall region to nearly isotropic in the outer layer.

By integrating the index-of-refraction field to various wall-normal positions and applying statistical analysis, the relative optical importance of different flow regions is compared. It is found that wavefront distortions are predominantly caused by the logarithmic layer and wake region, with the contribution peak located in the wake region due to both large density fluctuation magnitude and large correlation length there. Contributions from the viscous sublayer and buffer layer are small, especially for high-Reynolds-number flows. To investigate the flow-scale effect, low-pass filters with various filter widths are applied to the density field for the highest Reynolds-number case, and the optical distortions are calculated using the filtered density field. A comparison of time-averaged r.m.s. and power spectral density of OPD with and without density filtering show that small-scale turbulence contributes to the high-frequency content of OPD but has little effect on the low-frequency content and the overall magnitude. Therefore, small-scale turbulence is optically inactive, in agreement with previous numerical and experimental results for other types of aero-optical flows.

The elevation-angle dependence has been investigated by calculating OPD_{rms} along optical paths at different angles through the boundary layer. The anisotropic property of the turbulent boundary layer renders the optical distortions dependent on the direction of propagation. An optical beam is distorted more severely when its propagation path is tilted toward downstream than upstream at the same angle with respect to the wall-normal direction, in agreement with previous experimental findings (Cress *et al.* 2008) and numerical solutions for homogeneous turbulent flows with uniform mean shear (Truman & Lee 1990). A correlation analysis of the fluctuating density field confirms that the correlation length is larger along downstream-tilted optical paths than upstream-tilted ones, which accounts for the difference in distortion levels.

As the most important statistical model for aero-optics, Sutton's linking equation is examined regarding its applicability to boundary-layer flows. Based on a rigorous derivation, the approximations involved in the linking equation are identified, and the proper density length scale to be used in the equation is clarified. It should be defined in the form for homogeneous turbulent flows and account for the finite integration bounds. With the proper definition of correlation length scale, the linking equation predicts boundary-layer aero-optics in excellent agreement with directly integrated results.

Acknowledgements

REFERENCES

ADRIAN, R. J. 2007 Haripin vortex organization in wall turbulence. *Phys. Fluids* **19**, 1–16.

BODONY, D. 2006 Analysis of sponge zones for computational fluid mechanics. *J. Comput. Phys.* **212**, 681–702.

BUCKNER, A., GORDEYEV, S. & JUMPER, E. J. 2005 Optical aberrations caused by transonic attached boundary layers: underlying flow structure. *AIAA Paper* 2005–0752.

CASSADY, P. E., BIRCH, S. F. & TERRY, P. J. 1989 Aero-optical analysis of compressible flow over an open cavity. *AIAA J.* **27**, 758–762.

CHOI, H. & MOIN, P. 1990 On the space–time characteristics of wall-pressure fluctuations. *Phys. Fluids* A **2**, 1450–1460.

CRESS, J. 2010 Optical aberrations caused by coherent structures in a subsonic, compressible, turbulent boundary layer. PhD thesis, University of Notre Dame.

CRESS, J., GORDEYEV, S. & JUMPER, E. J. 2010 Aero-optical measurements in a heated, subsonic, turbulent boundary layer. *AIAA Paper* 2010–0434.

CRESS, J., GORDEYEV, S., POST, M. & JUMPER, E. J. 2008 Aero-optical measurements in a turbulent, subsonic boundary layer at different elevation angles. *AIAA Paper* 2008–4214.

DEGRAAFF, D. & EATON, J. 2000 Reynolds-number scaling of the flat-plate turbulent boundary layer. *J. Fluid Mech.* **422**, 319–346.

FITZGERALD, E. J. & JUMPER, E. J. 2004 The optical distortion mechanism in a nearly incompressible free shear layer. *J. Fluid Mech.* **512**, 153–189.

GARNIER, E., ADAMS, N. & SAGAUT, P. 2009 *Large Eddy Simulation for Compressible Flows*. Springer.

GEARY, J. M. 1995 *Introduction to Wavefront Sensors*. SPIE Press.

GILBERT, K. G. & OTTEN, L. J. (Eds) 1982 *Aero-Optical Phenomena*, Progress in Astronautics and Aeronautics. AIAA.

GLADSTONE, J. H. & DALE, T. P. 1863 Researches on the refraction, dispersion, and sensitivities of liquids. *Phil. Trans. R. Soc. Lond.* **153**, 317–343.

GORDEYEV, S. & JUMPER, E. J. 2010 Fluid dynamics and aero-optics of turrets. *Prog. Aerosp. Sci.* **46**, 388–400.

GORDEYEV, S., JUMPER, E. J. & HAYDEN, T. 2011 Aero-optics of supersonic boundary layers. *AIAA Paper* 2011–1325.

GORDEYEV, S., JUMPER, E. J., NG, T. T. & CAIN, A. B. 2003 Aero-optical characteristics of compressible subsonic turbulent boundary layer. *AIAA Paper* 2003–3606.

HAVENER, G. 1992 Optical wave front variance: a study on analytic models in use today. *AIAA Paper* 92–0654.

HUGO, R. J. & JUMPER, E. J. 2000 Applicability of the aero-optic linking equation to a high coherent, transitional shear layer. *Appl. Opt.* **39**, 4392–4401.

ISRAELI, M. & ORSZAG, S. 1981 Approximation of radiation boundary conditions. *J. Comput. Phys.* **41**, 115–135.

JUMPER, E. J. & FITZGERALD, E. J. 2001 Recent advances in aero-optics. *Prog. Aerosp. Sci.* **37**, 299–339.

LIEPMANN, H. W. 1952 Deflection and diffusion of a light ray passing through a boundary layer. *Tech. Rep.* SM-14397. Douglas Aircraft Company, Santa Monica Division, Santa Monica, CA.

LILLY, D. K. 1992 A proposed modification of the Germano subgrid-scale closure method. *Phys. Fluids* **4**, 633–635.

LUND, T. S., WU, X. & SQUIRES, K. 1998 Generation of turbulent inflow data for spatially-developing boundary layer simulations. *J. Comput. Phys.* **140**, 233–258.

MAHAJAN, V. N. 1983 Strehl ratio for primary aberrations in terms of their aberration variance. *J. Opt. Soc. Am.* **73**, 860–861.

MALLEY, M. M., SUTTON, G. W. & KINCHELOE, N. 1992 Beam-jitter measurements of turbulent aero-optical path differences. *Appl. Opt.* **31**, 4440–4443.

MANI, A., MOIN, P. & WANG, M. 2009 Computational study of optical distortions by separated shear layers and turbulent wakes. *J. Fluid Mech.* **625**, 273–298.

MANI, A., WANG, M. & MOIN, P. 2006 Statistical description of free-space propagation for highly aberrated optical beams. *J. Opt. Soc. Am.* A **23**, 3027–3035.

MANI, A., WANG, M. & MOIN, P. 2008 Resolutions requirements for aero-optical simulations. *J. Comput. Phys.* **227**, 9008–9020.

MOIN, P., SQUIRES, K., CABOT, W. & LEE, S. 1991 A dynamic subgrid-scale model for compressible turbulence and scalar transport. *Phys. Fluids* **11**, 2746–2757.

MONIN, A. S. & YAGLOM, A. M. 1975 *Statistical Fluid Mechanics: Mechanics of Turbulence, vol. II.* MIT.

ROBINSON, S. K. 1991 Coherent motions in the turbulent boundary layer. *Annu. Rev. Fluid Mech.* **23**, 601–639.

SHOEYBI, M., SVARD, M., HAM, F. E. & MOIN, P. 2010 An adaptive implicit-explicit scheme for the DNS and LES of compressible flows on unstructured grids. *J. Comput. Phys.* **229**, 5944–5965.

STEINMETZ, W. J. 1982 Second moments of optical degradation due to a thin turbulent layer. In *Aero-Optical Phenomena* (ed. K. G. Gilbert & L. J. Otten), *Progress in Astronautics and Aeronautics*, vol. 80, pp. 78–100. AIAA.

SUTTON, G. W. 1985 Aero-optical foundations and applications. *AIAA J.* **23**, 1525–1537.

TROMEUR, E., GARNIER, E. & SAGAUT, P. 2006a Analysis of the Sutton model for aero-optical properties of compressible boundary layers. *J. Fluids Engng-Trans. ASME* **128**, 239–246.

TROMEUR, E., GARNIER, E. & SAGAUT, P. 2006b Large-eddy simulation of aero-optical effects in a spatially developing turbulent boundary layer. *J. Turbul.* **7**, 1–28.

TROMEUR, E., GARNIER, E., SAGAUT, P. & BASDEVANT, C. 2003 Large eddy simulation of aero-optical effects in a turbulent boundary layer. *J. Turbul.* **4**, 1–22.

TRUMAN, C. R. 1992 The influence of turbulent structure on optical phase distortion through turbulent shear flows. *AIAA Paper* 92–2817.

TRUMAN, C. R. & LEE, M. J. 1990 Effects of organized turbulence structures on the phase distortion in a coherent optical beam propagation through a turbulence shear flow. *Phys. Fluids* **2**, 851–857.

TSAI, Y. P. & CHRISTIANSEN, W. H. 1990 Two-dimensional numerical simulation of shear-layer optics. *AIAA J.* **28**, 2092–2097.

TYSON, R. K. 1997 *Principles of Adaptive Optics*, 2nd edn. Academic.

URBIN, G. & KNIGHT, D. 2001 Large-eddy simulation of a supersonic boundary layer using an unstructured grid. *AIAA J.* **39**, 1288–1295.

WANG, M., MANI, A. & GORDEYEV, S. 2012 Physics and computation of aero-optics. *Annu. Rev. Fluid Mech.* **44**, 299–321.

WITTICH, D., GORDEYEV, S. & JUMPER, E. J. 2007 Revised scaling of optical distortions caused by compressible, subsonic turbulent boundary layers. *AIAA Paper* 2007-4009.

WYCKHAM, C. M. & SMITS, A. 2009 Aero-optic distortion in transonic and hypersonic turbulent boundary layers. *AIAA J.* **47**, 2158–2168.

ZUBAIR, F. R. & CATRAKIS, H. J. 2007 Aero-optical resolution robustness in turbulent separated shear layers at large Reynolds numbers. *AIAA J.* **45**, 2721–2728.